Journal of Materials Chemistry A

PAPER

View Article Online
View Journal

Cite this: DOI: 10.1039/c8ta10351h

Stable lithium–sulfur full cells enabled by dual functional and interconnected mesocarbon arrays†

Daxian Cao, ‡[a] Yucong Jiao,‡[a] Qingfu Cai,[b] Dandan Han,[b] Qing Zhang,[a] Yi Ma,[a] Angang Dong [b] and Hongli Zhu *[a]

Received 28th October 2018
Accepted 14th January 2019

DOI: 10.1039/c8ta10351h

rsc.li/materials-a

Lithium metal–sulfur (Li–S) batteries have gained wide attention due to extremely high energy density, but their application was hindered by the challenges related to both the sulfur cathode and Li anode. Herein, we designed dual functional, highly ordered, and interconnected mesoporous carbon (MPC) to address the challenges related to the cathode and anode simultaneously. On the anode, a thin layer of MPC annealed at 500 °C (MPC-500) was introduced to mechanically suppress Li dendrite growth, which provided interfacial protection on the Li metal and stabilized the Li plating/stripping. This novel anode showed excellent cycling stability at a high current density of 3 mA cm^{-2}. On the cathode, MPC annealed at 1300 °C (MPC-1300) was utilized to confine sulfur. The interconnected mesoporous carbon sphere with a large surface area significantly alleviated the shuttle effect, which contributes to the cycling stability of the Li–S battery. Meanwhile, the conductive carbon promotes electron transfer. When a Li–S full cell was assembled with MPC-500 and MPC-1300 as an anode interface layer and cathode additive, respectively, an exceptional reversible capacity of 607 mA h g^{-1} was achieved at a discharge rate of 1 C (1675 mA g^{-1}) and maintained at a high capacity retention of 87.5% after 100 cycles.

1 Introduction

The search for advanced materials with high energy density and low cost for sustainable energy storage is crucial due to the increasing demand for energy.[1–3] Conventional lithium-ion batteries (LIBs) with transition metal oxide cathodes and graphite anodes have a limited energy density of less than 250 W h kg^{-1}.[4] Lithium metal is regarded as the ideal choice of anode material due to its highest theoretical capacity of 3860 mA h g^{-1} (graphite is 372 mA h g^{-1}), lowest electrochemical potential of −3.04 V *versus* the standard hydrogen electrode (SHE), and lightweight (density is 0.53 g cm^{-3}).[5–9] Meanwhile, sulfur as a cathode material possesses an outstanding theoretical specific capacity of 1675 mA h g^{-1} with an energy density as high as 2600 W h kg^{-1}, and it is naturally abundant and cost-effective (~$150 ton^{-1}). Therefore pairing the lithium metal anode with the sulfur cathode has the potential to reach a high energy density of 500 W h kg^{-1}.[10–13]

However, several challenges related to both the anode and cathode need to be tackled for the large-scale commercialization of Li–S batteries.[14–16] On the Li anode side, the unstable solid electrolyte interface (SEI), infinite volume change, and uncontrollable growth of lithium dendrite cause unstable Li stripping/plating. The drastic volume change during cycling results in the repeated breaking and re-forming of the SEI, which consumes Li^+ ions continuously and deteriorates the Coulombic efficiency (CE) of cycling. Moreover, the sharp lithium dendrites formed in the cycling process penetrate the separator and result in short-circuit.[6,17,18] Hence, a more uniform Li deposition/dissolution process on the lithium metal anode with extended cycling is required for a safer battery with high CE.[19] Introducing a protective layer on the surface of Li metal is an effective approach to suppress Li dendrite growth. A high mechanical strength, good chemical stability, and high ionic conductivity are desired for the interlayer materials.[20] Cui *et al.* reported that a thin layer of interconnected hollow carbon nanospheres could facilitate the formation of a stable SEI and lead to a uniform deposition of Li on Cu.[21] 2D materials such as graphene and BN were also investigated as excellent interfacial protections on Li metal.[22] As for the cathode side of Li–S batteries, sulfur suffers from problems arising from the extremely low electrical conductivity (5×10^{-30} S cm^{-1}), the shuttle effect induced by the dissolution of polysulfide and large volume expansion/shrinkage during discharge/charge.[23] The utilization of the active material and electrochemical reaction kinetics were greatly decreased because of the poor conductivity. Meanwhile, poor cycling stability and capacity degradation were inevitable because of the shuttle effect of polysulfide intermediates and volume change.[24–26] To date, confining sulfur

[a]Department of Mechanical and Industrial Engineering, Northeastern University, Boston, Massachusetts, 02115, USA. E-mail: h.zhu@neu.edu

[b]Department of Chemistry and Collaborative Innovation Center of Chemistry for Energy Materials, Fudan University, Shanghai, 200433, China

† Electronic supplementary information (ESI) available. See DOI: 10.1039/c8ta10351h

‡ D.C. and Y.J. contributed equally to this work.

in a conductive host is one of the most effective strategies to address these problems. Conductive carbon materials, such as graphene, carbon nanotubes, and porous carbon, have been employed as host materials to confine sulfur and improve electron transfer.[27–33] A host with a uniform pore diameter can confine the sulfur well when buffering the volume change. A large surface area of the host allows higher mass loading of sulfur and benefit electrolyte accessibility.

Inspired by the strategies aforementioned for the stabilization of the Li metal anode and sulfur cathode, we propose dual-functional MPC with the optimization of the anode and cathode simultaneously. Highly ordered and interconnected MPC-500 showed good chemical stability and a high mechanical strength to effectively suppress the Li dendrite growth and form a stable SEI for fast ion transfer. As to the cathode, MPC-1300, carbonized at a higher temperature, exhibited a large surface area of 1198 $m^2\ g^{-1}$ and a high conductivity due to the higher graphitization degree. The large surface area and interconnected pores provided sufficient space for trapping sulfur and accommodating the volume change. Meanwhile, the graphitic walls of MPC-1300 could facilitate electron transportation and enhance rate performance.

As a result, more stable stripping/plating cycling was achieved for Li metal with the protection of MPC-500, compared to unprotected Li metal. A high CE of 98% was maintained for more than 200 cycles at a current density of 1 mA cm^{-2} and an areal capacity of 1 mA h cm^{-2}. At a higher current density of 3 mA cm^{-2} and an areal capacity of 3 mA h cm^{-2}, the Li/MPC-500 anode demonstrated stable stripping/plating cycling for 300 cycles with a greatly reduced overpotential compared to unprotected Li metal. Combining the Li/MPC-500 anode and S/MPC-1300 cathode in a Li–S battery, a high capacity of 607 mA h g^{-1} was achieved at 1 C (1675 mA g^{-1}) and retained 87.5% of the initial capacity after 100 cycles, which is much higher and more stable than the control group without optimization with MPC. With the dual-functional MPC, we alleviated several issues related to both the anode and cathode in the Li–S full cell simultaneously, and a stable cycling performance of the Li–S full cell was achieved. Our method is an effective approach to improve the stability and safety of Li–S batteries for large-scale applications.

2 Results and discussion

Fig. 1 illustrates the several challenges in conventional Li–S batteries and the structural features of our novel Li–S batteries with dual-functional MPC. In the conventional Li–S battery shown in Fig. 1a, as we mentioned, the severe dendrite growth, the polysulfide induced shuttle effect, and the poor conductivity of sulfur significantly limit the application of Li–S batteries. To address these issues, we designed a novel Li–S battery by introducing the dual-functional MPC into both the anode and cathode (Fig. 1b). In the anode part, MPC-500 was employed to mechanically suppress lithium dendrite growth and form a stable SEI with sufficient ion transfer pathways. As to the cathode part, MPC-1300, derived from carbonization at 1300 °C, was utilized to host sulfur. With this interconnected and ordered porous structure, the long chain polysulfides could be trapped effectively, while the electrolyte can easily access the active material to improve the utilization of the active material. The carbon walls with higher graphitization could enhance the conductivity of the electrode. As a result, the as-designed battery is expected to provide excellent cycling stability at high current density.

The highly ordered MPC was fabricated by a typical method reported by Dong's group before, with a highly ordered iron oxide superlattice framework as the matrix.[2,34] Fig. 2 shows the structural characterization of the as-prepared MPC-500 and MPC-1300. The transmission electron microscopy (TEM) images shown in Fig. 2a–c revealed that the carbon structure in MPC-500 is formed by a long-range ordered hollow carbon sphere, and the pore size is around 10 nm, similar to the size of iron oxide nanoparticles. It should be noted that these carbon spheres are not isolated, but interconnected by fine pores on the carbon wall, causing percolation for ion transfer. MPC-500 has a favorable structure as a protective layer on the Li metal surface. As shown in Fig. 2d–e, MPC-1300 maintained the highly ordered, interconnected structure of MPC-500, indicating the robustness of this structure with increasing temperature. These pores can well confine sulfur and buffer the volume change. It should be noted that the carbon walls of MPC-1300 were partially crystallized and the size of the pores decreased a little compared with MPC-500. From the HRTEM image, well-crystalline graphene layers were very clear, implying good electronic conductivity of this material.

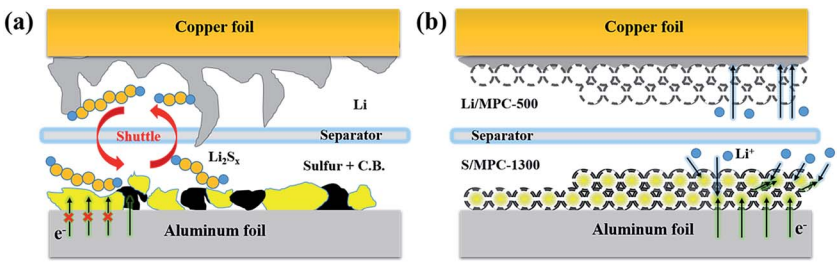

Fig. 1 Schematic representation illustrating the Li–S batteries with/without the optimization of MPC. (a) Control Li–S battery assembled with bare Li on Cu as the anode, and sulfur composited with carbon black and binder as the cathode. The dendrite problem, shuttle effect and poor conductivity of sulfur are conceptually depicted. (b) Novel Li–S battery with dual-functional MPC. The cathode was sulfur confined in MPC-1300, while the anode was MPC-500-covered Li on Cu. The challenges in conventional Li–S batteries were correspondingly addressed.

The graphitization degree of both MPC-500 and MPC-1300 was investigated using Raman spectroscopy, as shown in Fig. 2g. The two prominent peaks located at 1361 and 1583 cm^{-1} for MPC-500 correspond to the D and G peaks of carbon, respectively. The D and G peaks were related to the disordered structure of carbon with sp^3 hybridization and the stretching mode of carbon with sp^2 hybridization, respectively.[35] As to MPC-1300, the D peak and G peak slightly shift to 1338 and 1595 cm^{-1} compared with MPC-500. The intensity ratio of D and G peaks (I_D/I_G, peak area ratio) was used to determine the crystallization degree of carbon. With increasing annealing temperature, the I_D/I_G ratio decreases from 2.2 to 1.6 for MPC-500 and MPC-1300, respectively, which agrees well with the partial graphitization of the carbon walls. Fig. 2h and i show the pore size distribution of MPC-500 and MPC-1300, respectively. The inset figures show N_2 adsorption–desorption isotherms. In MPC-500, the large pores located at 12.7 nm were derived from 12 nm Fe_3O_4 nanocrystals, while the pores with 3 nm in width resulted from the small openings on the carbon walls. The N_2 adsorption–desorption curve delivered a typical type-IV isotherm, where the large hysteresis loop implies a caged mesoporous structure with tiny channels on the walls. The Brunauer–Emmett–Teller (BET) surface area of MPC-500 is 1134 $m^2 g^{-1}$. Compared to MPC-500, the pore size of MPC-1300 decreased to 9.2 nm due to the partial contraction occurred during calcination. A similar N_2 adsorption–desorption curve was observed, while the BET surface area increased to 1198 $m^2 g^{-1}$. As we mentioned, these structural features and large surface area play a key role in improving the performance of Li–S batteries.

Coulombic efficiency (CE) was evaluated to compare the plating and stripping behavior of Li on a bare copper electrode (Cu) and on Cu coated with MPC-500 (Cu/MPC-500). In a typical measurement, a fixed amount of Li was deposited on the working electrode first, and then stripped out with a cutoff voltage of 1 V at the same current density. This process was repeated several times, and the CE was calculated based on the capacity ratio of stripping/plating. As Fig. 3a displays, at a current density of 1 mA cm^{-2} and an areal charge capacity of 1 mA h cm^{-2}, the Cu/MPC-500 electrode could keep an extraordinarily high CE of ~98% for over 200 cycles. In contrast, the CE of the Cu electrode started to decrease from the beginning, and was only 70% after 100 cycles, from where the CE fluctuated a lot and dropped down to zero after 170 cycles. Fig. 3b shows the plating/stripping curves of Li on Cu and Cu/MPC-500 electrodes of the 1st and 160th cycles. It is obvious

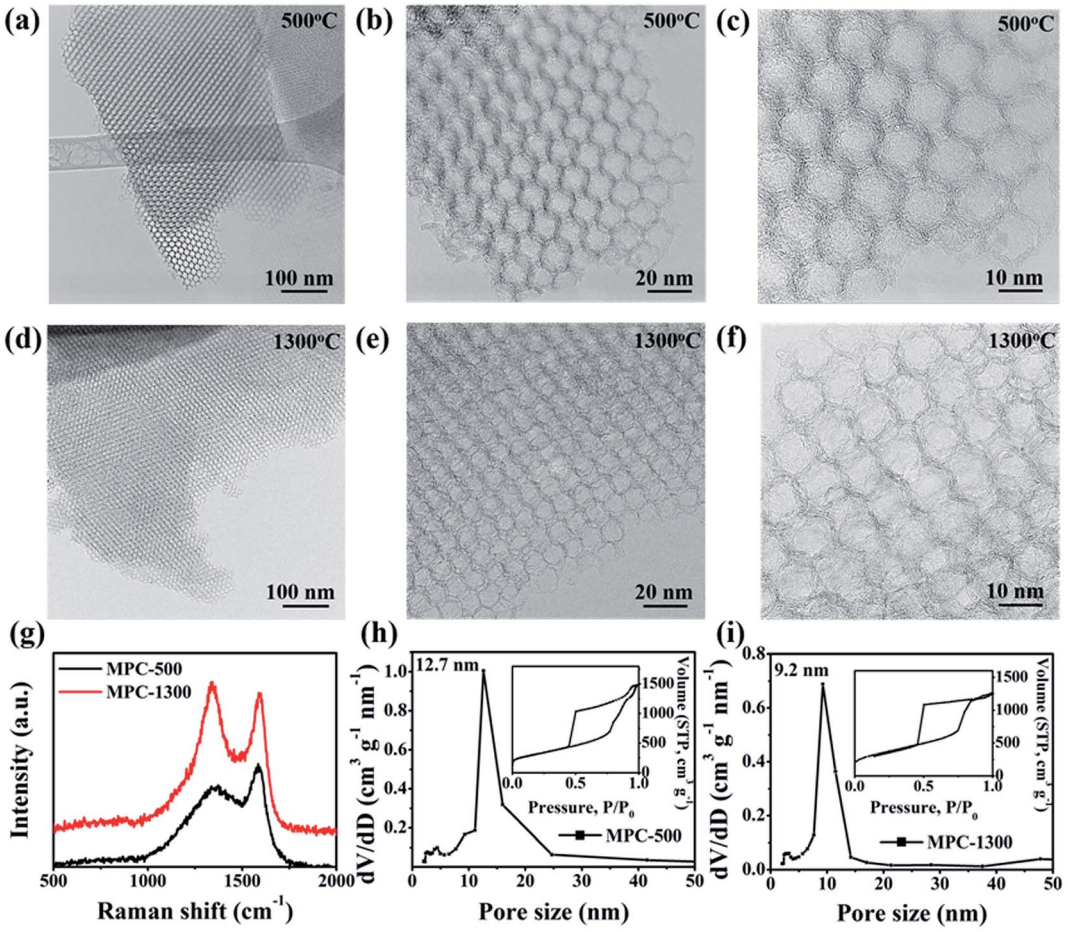

Fig. 2 Characterization of MPC-500 and MPC-1300. TEM images to show the highly ordered structure of (a–c) MPC-500 and (d–f) MPC-1300. (g) Raman spectra of MPC-500 and MPC-1300, showing the crystallization degree revolution. The pore size distribution of (h) MPC-500 and (i) MPC-1300, while the insets show the N_2 adsorption/desorption isotherms.

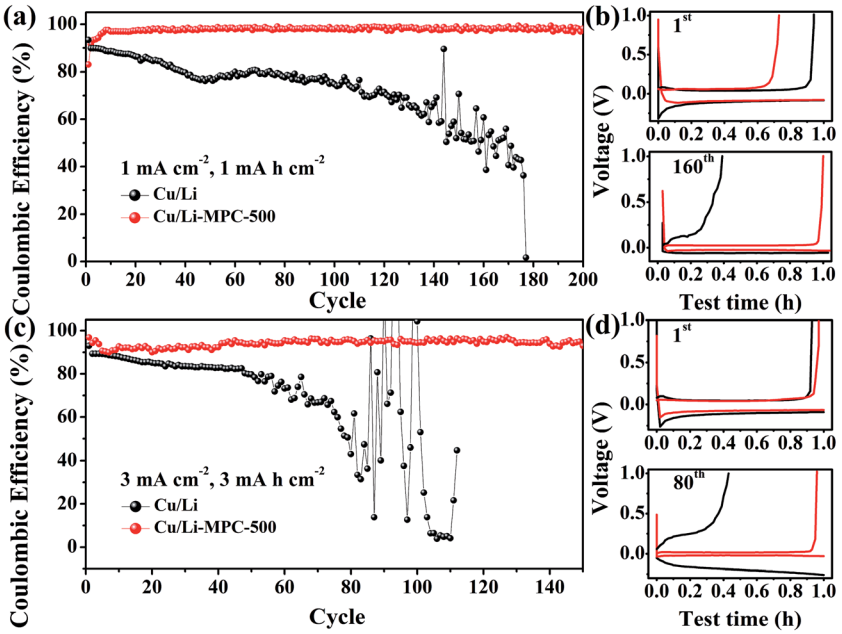

Fig. 3 The CE comparison of Cu/MPC-500 and Cu electrodes (a) with an areal charge of 1 mA h cm^{-2} at a current density of 1 mA cm^{-2}, and (c) with an areal charge of 3 mA h cm^{-2} at a current density of 3 mA cm^{-2}. The cutoff voltage in each cycle was 1 V. The corresponding plating/stripping curves in different cycles with a current density of (b) 1 mA cm^{-2} and (d) 3 mA cm^{-2}.

that Cu/MPC-500 showed a much lower overpotential than the Cu electrode. The stripping capacity of Cu/MPC-500 was a little lower than that of Cu initially, which could be attributed to the stable SEI layer formed on the Cu electrode. After 160 cycles, the stripping capacity of the Cu electrode decreased a lot and the curve fluctuated. In comparison, Cu/MPC-500 delivered a very stable and high CE of around 98%. When the current density was increased to 3 mA cm^{-2} with an areal charge of 3 mA h cm^{-2}, the Cu/MPC-500 electrode exhibited a high CE of 95% and maintained it for 150 cycles, while the Cu electrode showed a fast decaying CE to 40% in 80 cycles (Fig. 3c). Fig. 3d displays the corresponding plating/stripping curves of the 1^{st} and 80^{th} cycles. A lower overpotential and remarkably more stable deposition/dissolution were achieved with the Cu/MPC-500 electrode compared to the Cu electrode. These sharp differences proved that MPC-500 provides effective protection on the Cu for a more uniform and stable Li plating/stripping process. These benefits of MPC-500 could be ascribed to the high mechanical strength of the material and the highly ordered, interconnected pores of the structure.

To investigate the cycling stability of electrodes deposited with Li, a fixed amount of Li was pre-deposited on bare Cu and Cu/MPC-500 to form Cu–Li and Cu/Li-MPC-500 anodes, followed by a repeated plating/stripping process at the same current density and areal charge in each cycle (Fig. 4). It should be noted that Li foil was used as the counter electrode in this measurement. As shown in Fig. 4a, pre-deposited with an areal capacity of 10 mA h cm^{-2} of lithium and plated/stripped at a current density of 1 mA cm^{-2} and an areal charge of 1 mA h cm^{-2}, Cu/Li-MPC-500 showed a stable cycling performance over 300 h, while Cu/Li showed dramatically increased voltage hysteresis in only 60 h and failed quickly. Fig. 4b and c compare the plating/stripping curves in the pre-deposition process and during the cycling. In the initial stage, the nucleation overpotential of Cu/MPC-500 (0.10 V) is much smaller compared to that of the Cu electrode (0.28 V). During cycling, the lithium plating/stripping polarization of Cu/Li-MPC-500 was smaller than 30 mV, while it was higher than 50 mV for the Cu electrode. For the Cu/Li electrode, the bad performance could be ascribed to the continuous breakdown and rebuild of a SEI film on the copper electrode, and the formation of lithium dendrites through and along the cracks of the films. In contrast, Cu/Li-MPC-500 shows an excellent stable cycling performance and lower overpotential. This could be attributed to the much stable SEI layer induced by the MPC layer, which suppresses lithium dendrite formation. Pre-deposited with 18 mA h cm^{-2} of Li, Fig. 4d shows the cycling performance of Cu/Li and Cu/Li-MPC-500 at a higher current density of 3 mA cm^{-2} and an areal charge of 3 mA h cm^{-2}. It is obvious that overpotential increased significantly in Cu/Li in only 30 h, while Cu/Li-MPC-500 showed a more stable cycling performance. Comparing the plating curves in an initial deposition, the voltage drop of lithium plating on Cu/MPC-500 is still much smaller than that on bare Cu (Fig. 4e). After 50 h, the stripping curves of Cu/Li showed more fluctuation and big voltage hysteresis, while the voltage was much smoother in Cu/Li-MPC-500 (Fig. 4f). These results further confirmed that the introducing of MPC-500 on Cu could help to form a stable SEI and stabilize Li.

To confirm our proposed mechanisms for the cycling performance, and further understand the electrochemical lithium plating and stripping behavior, scanning electron microscopy (SEM) was employed to investigate the morphology of Cu and Cu/MPC-500 electrodes before and after cycling (Fig. 5). The SEM images of Cu before lithium plating showed

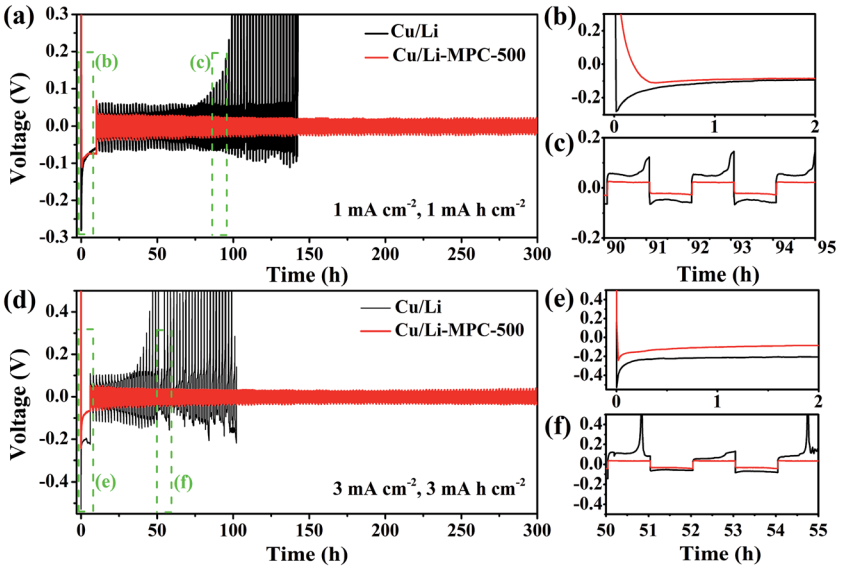

Fig. 4 The comparison of the cycling performance (a) of Cu/Li and Cu/Li-MPC-500 anodes at a current density of 1 mA cm^{-2} and an areal charge of 1 mA h cm^{-2}, and the plating/stripping curves (b) in the initial stage and (c) between 90 to 95 h, (d) at a current density of 3 mA cm^{-2} and an areal charge of 3 mA h cm^{-2}, and the plating/stripping curves (e) in the initial stage and (f) between 50 to 55 h.

that Cu exhibited a very flat surface (Fig. 5a). After being deposited with Li for 10 h at a current density of 1 mA cm^{-2}, obviously, there were large parts of lithium dendrites on the surface of Cu/Li, which was caused by the uneven lithium deposition (Fig. 5b). The whole Cu electrode was covered by Li, as shown in the inset. After continuously stripping/plating for 70 h, lots of sharp dendrites grew out of the copper surface, which could trigger the formation of dead lithium and consume much more electrolyte. These results related well with the cycling performance, where the voltage hysteresis sharply increased after 70 hours (Fig. 5c). However, with the protection of MPC-500, the dendrite issue of the Cu electrode was well addressed. Before the deposition of Li, MPC-500 covered the Cu uniformly and showed no un-covered part. The pores of MPC-500 allow the electrolyte to access Cu (Fig. 5d). After plating Li for 10 h at a current density of 1 mA cm^{-2}, as shown in Fig. 5e, the MPC-500 layer still covered Cu uniformly, and no lithium dendrite was observed. The inset digital image of the electrode confirmed that the Li was deposited under the MPC-500 layer and no penetration occurred. Fig. 5f shows the SEM image of Cu/Li-MPC-500 cycled after 70 hours at a current density of 1 mA cm^{-2}. Different from the Cu electrode, no dendrite was observed on the carbon surface by SEM, which agrees with the better performance of Cu/Li-MPC-500 as shown in Fig. 4. The inset image displays the corresponding cross section of the Cu/Li-MPC-500 electrode. It can be observed that there was a layer of Li deposited underneath the MPC-500 layer. In this situation, the MPC behaved more as a protecting layer to

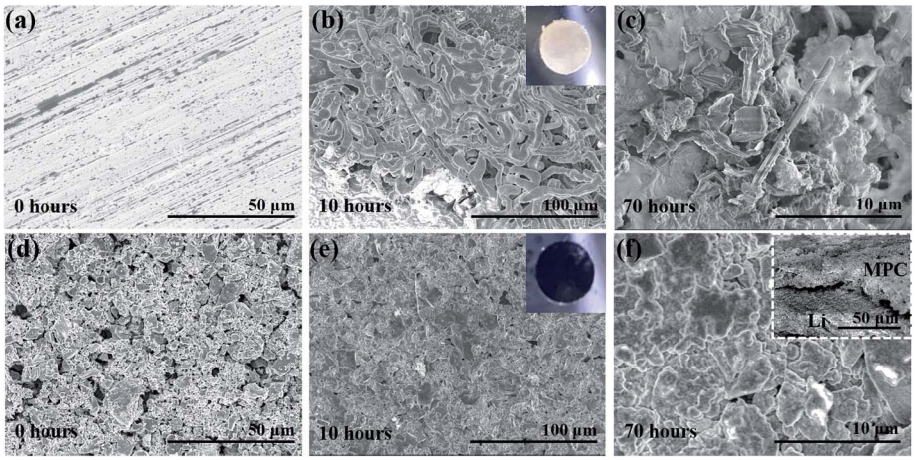

Fig. 5 SEM images of the bare Cu electrode and Cu/MPC-500 before and after different lithium plating and stripping procedures. Cu electrode (a) before cycling; (b) after plating for 10 hours; and (c) after cycling for 70 hours. Cu/MPC-500 electrode (d) before cycling; (e) after plating for 10 hours; and (f) after cycling for 70 cycles. Inset images in (b and c) show the digital images of the corresponding electrodes. Inset image in (f) shows the expansion of the morphology of the electrode cross section.

suppress the lithium dendrite growth and prevent the surface SEI layer from cracking. It has been reported that the low conductivity of the carbon lacking of a long-range order can reduce direct Li deposition onto the carbon.[21] In the initial deposition process, Li ions gradually react with the graphitic regions in a lithiated process and form a stable SEI. The MPC will not hinder the accessibility of the electrolyte to the Cu, but leads to a more uniform distribution of the electrolyte. As a result, the Li will homogeneously deposit/dissolve on the Cu during the plating/stripping process. This could explain the excellent cycling stability after long cycling of 300 hours.

As we mentioned before, the host for the sulfur cathode should have a high conductivity for electron transfer. MPC-1300 which was produced by carbonizing MPC at 1300 °C for 2 h was employed to confine the sulfur. Sulfur was embedded in MPC-1300 *via* a melt-diffusion method according to Dong's work.[36] As shown in the SEM and TEM images in Fig. S1,† MPC-1300 maintained the highly ordered structure well after the infiltration of sulfur with a mass loading of 65%. Energy dispersive X-ray spectroscopy (EDX) maps of S/MPC-1300 further proved that sulfur was homogeneously distributed in the MPC structure, as shown in Fig. 6a–c. As a result, full cells with Al/S-MPC-1300 as the cathode and Cu/Li-MPC-500 as the anode were assembled to evaluate the dual function of MPC in the stabilization of Li–S batteries. In comparison, a control group was also prepared, where sulfur mixed with carbon black and Cu deposited with Li were chosen as the cathode and anode, respectively. The electrochemical behavior was evaluated by cyclic voltammetry (CV) at a scan rate of 0.1 mV s^{-1}. Fig. 6d shows the CV curves of the Li–S battery with the MPC-containing cathode and anode for the first five cycles. The obvious reduction and oxidation peaks correspond to typical redox reactions between Li and sulfur. In the first cathodic scan, the peak at ~2.28 V is attributed to the reduction of S_8 molecules into lithium polysulfides with long

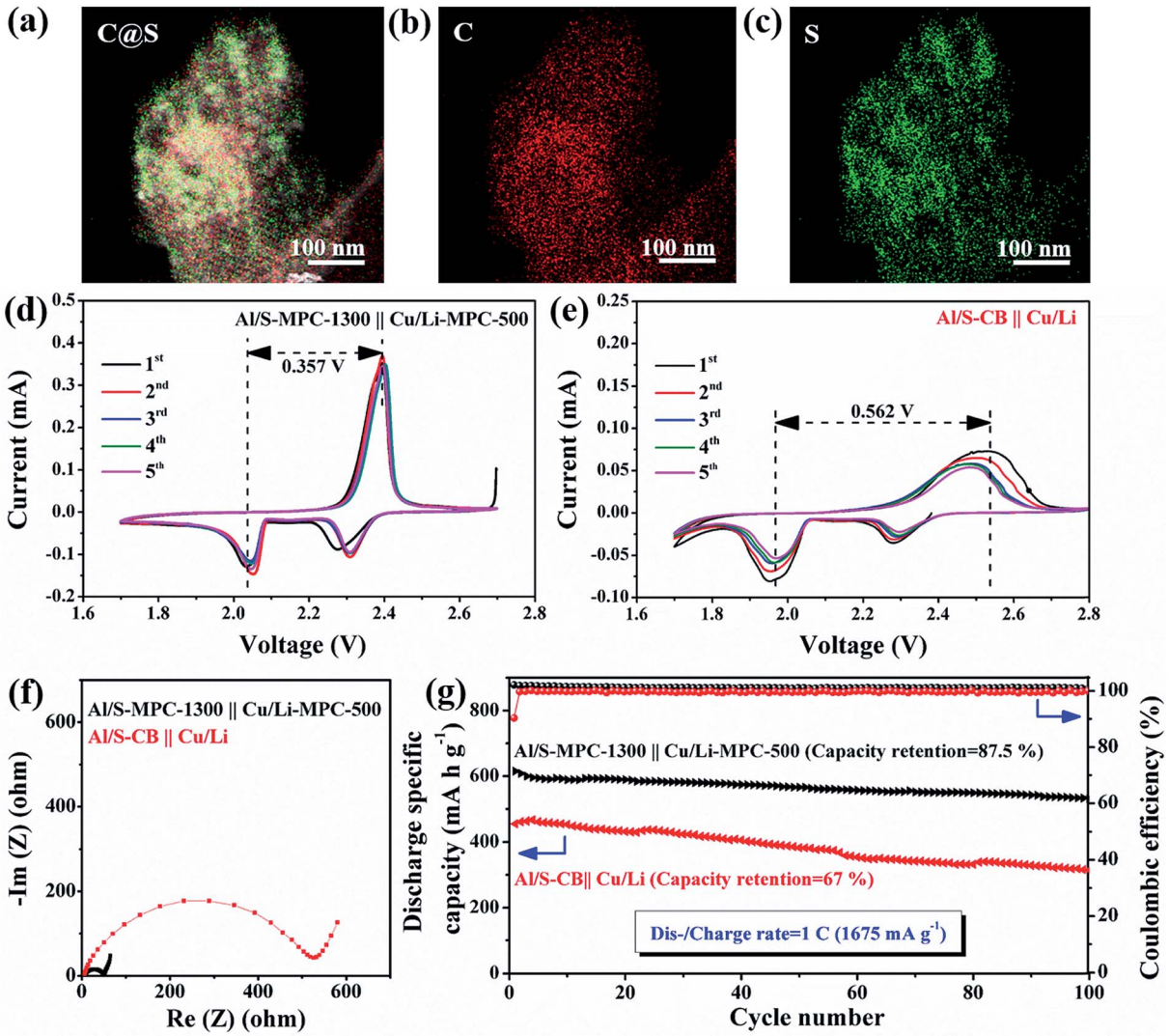

Fig. 6 Morphology characterization of S/MPC-1300 and corresponding battery performance in comparison with the control group; (a) EDX mapping of S/MPC-1300; (b) EDX mapping of carbon in the MPC structure; (c) EDX mapping of sulfur in the MPC structure, showing no aggregation of sulfur; (d) CV curves of Li–S batteries optimized with MPC; (e) CV curves of control Li–S batteries. (f) Nyquist plots of Li–S batteries with/without optimization of MPC; (g) Cycling stability comparison between Li–S batteries with/without the optimization of MPC at a high dis-/charge rate of 1C (1675 mA g^{-1}).

chains (Li_2S_n, $4 \leq n < 8$), while the peak centered at 2.04 V resulted from further lithiation of Li_2S_n ($4 \leq n < 8$) to form short-chain lithium polysulfides (Li_2S_n, $n \leq 2$).[37,38] In the reversed scan, the lithium polysulfides were oxidized to elemental S_8, and this reaction occurred at ~2.38 V.[38,39] In the subsequent cycles, the current intensity and peak positions were similar, implying that the introducing of MPC into both electrodes could effectively stabilize the Li–S battery. In contrast, the CV curves of the control group displayed ill-defined redox peaks and severe polarization, which proves the sluggish reaction kinetics caused by the poor conductivity. Furthermore, the current intensity of the peaks gradually decreased as the cycling proceeds, which corresponds to the loss of active materials due to the shuttle effect. Electrochemical impedance spectroscopy (EIS) measurements were conducted to elucidate the electrochemical performance (Fig. 6f). The Nyquist plots of both batteries include a semicircle in the high frequency region, and a straight line in the low frequency region, which can be assigned to the charge transfer resistance (R_{ct}) and ion diffusion resistance, respectively. It is obvious that a much lower R_{ct} of 52 Ω was achieved in the optimized cell, likely due to both the high electrical conductivity of MPC-1300 and the high ion accessibility that resulted from the enhanced graphitization degree and large surface area. The rate performance is compared in Fig. S2,† and it is obvious that the cell with MPC optimization possesses much higher capacity than the one without optimization. Cycling stability was further investigated at a high dis-/charge rate of 1C (corresponding to 1675 mA g^{-1}). It should be noted that, before the cycling at 1C, an activation at 0.05C was performed for 3 cycles (data not shown). As Fig. 6g shows, with both electrodes benefiting from the unique structure of MPC, the battery exhibits a high discharge specific capacity of 607 mA h g^{-1} in the initial stage with a high capacity retention of 87.5% after 100 cycles. The charge/discharge profiles of the optimized cell are shown in Fig. S3,† where the plateaus well agreed with the CV curves and the capacity showed no obvious decay after 100 cycles. In comparison, with the same current density, the control group showed a much lower discharge specific capacity of 478 mA h g^{-1} in the initial discharge which quickly decayed to 320 mA h g^{-1} after 100 cycles with a capacity retention of 67%. Obviously, the CE of the MPC-optimized cell is close to 100% and much higher than that of the control group. To demonstrate the significance of the stabilization in the anode, we assemble a cell with S/MPC-1300 as the cathode and Li foil as the anode (Fig. S4†). When charging/discharging at the same rate at 1C for 100 cycles, the specific discharge capacity decreased from 620 mA h g^{-1} to 397 mA h g^{-1}, with a capacity retention of only 64%. Therefore, the highly stable performance of the MPC-optimized cell was attributed to the stabilization effect of MPC on both the Li metal anode (with MPC-500) and sulfur cathode (with MPC-1300).

3 Conclusions

In summary, for the first time, we designed dual-functional mesoporous carbon applied to both the anode (MPC-500) and cathode (MPC-1300) in Li–S batteries. When applied in a Li–S battery, the dual-functional MPC demonstrates several advantages: (1) the highly ordered and interconnected structure of MPC-500 functions as a protective layer to effectively suppress the Li dendrite formation; (2) the large surface area and confined pores could trap a high mass loading of sulfur to reduce the shuttle effect and increase the utilization of active material; (3) MPC-1300 annealed at a higher temperature of 1300 °C showed enhanced electric conductivity due to partial graphitization, which enhances the conductivity of the sulfur electrode and improve cycling performance at high current density. As a result, when MPC was applied to both the anode and cathode in Li–S batteries, a much higher and more stable cycling performance was achieved. In addition to Li–S batteries, this dual-functional material could be applied toward other Li metal based batteries such as Li–air batteries, to improve their stabilities in electrochemical energy storage.

4 Experimental section

4.1 Material synthesis

4.1.1 Synthesis of MPC-500, MPC-1300 and S/MPC-1300. The fabrication method for the highly ordered, interconnected MPC followed a typical strategy reported previously. Briefly, a 3D Fe_3O_4 superlattice was fabricated by the self-assembly of monodispersed and oleic acid capped Fe_3O_4. Then the superlattice was carbonized at 500 °C in an argon atmosphere for 2 hours to transform the surface oleic acid into carbon. Afterward, the Fe_3O_4 was etched with acid at room temperature while maintaining the ordered mesoporous carbon structure to obtain MPC-500. MPC-1300 was obtained after further annealing at 1300 °C for 2 h. S/MPC-1300 was prepared by a melt-diffusion method in an autoclave. Typically, 18 mg MPC-1300 and 33 mg sulfur were manually ground together, and the mixture was transferred to an autoclave. Then, the autoclave was kept in a furnace for 24 hours at 155 °C in an argon atmosphere to obtain S/MPC-1300. There is no mass loss in the melt-diffusion process. Thus the mass loading of sulfur was calculated based on the weight ratio of sulfur in the initial precursor mixture.

4.1.2 Preparation of Cu/MPC-500 and Al/S-MPC-1300 electrodes. Both of the electrodes were prepared through a casting method. In detail, a slurry composed of MPC-500 and polyvinylidene-fluoride (PVDF) binder with a weight ratio of 9 : 1 in NMP was prepared and casted onto copper foil, followed by drying in a vacuum for 12 hours at 100 °C. After drying, the foil was punched into circular disks with a diameter of 10 mm for further use. The mass loading of each disk was ~0.5 mg cm^{-2}. Similarly, S/MPC-1300, carbon black, and PVDF with a weight ratio of 80 : 10 : 10 were dispersed in NMP and then casted onto Al foil. After drying, the foil was punched into circular disks with a diameter of 6.5 mm. The mass loading of each disk was ~2 mg cm^{-2}. In the control group, sulfur, carbon black, and PVDF with a weight ratio of 65 : 25 : 10 were dispersed in NMP to make a slurry and casted on Al foil to prepare an Al/S-CB cathode. The diameter and mass loading were the same as those of the Al/S-MPC-1300 sample.

4.2 Electrochemical measurements

All the electrochemical measurements were performed in CR-2025-type coin cells, which were assembled in a glovebox with the concentration of H_2O and O_2 lower than 0.1 ppm. The electrolyte was 1 M Li bis(trifluoromethanesulphonyl)-imide (LiTFSI) dissolved in DOL/DME (1 : 1 v/v) with 2 wt% Lithium nitrate. The separator used was a Celgard 2325. A LANDTH 8-channel tester was employed for the galvanostatic test. EIS was conducted using a Biologic SP150 potentiostat.

4.2.1 Coulombic efficiency (CE) measurement. In the CE measurement, Cu/MPC-500 or bare Cu was used as the working electrode, and Li foil was used as the counter/reference electrode. Prior to test, batteries were activated at a very low current of 10 μA between 0.01 and 1 V for 5 cycles to remove the surface contamination. Then, lithium was plated onto Cu/MPC-500 or bare Cu at a current density of 1 mA cm^{-2} and 3 mA cm^{-2}, for 1 hour, and charged back to a voltage cutoff of 1.0 V. The CE was calculated from the ratio of charge/discharge capacity of each cycle.

4.2.2 Cycling stability evaluation. For the cycling stability performance, Li with an areal charge of 10 mA h cm^{-2} and 18 mA h cm^{-2} was pre-deposited on Cu/MPC-500 and Cu to form Cu/Li-MPC-500 and Cu/Li anodes, respectively. Then the cells were discharged and charged at a current density of 1 mA cm^{-2} or 3 mA cm^{-2} with an areal charge of 1 and 3 mA h cm^{-2}, respectively.

4.2.3 Li–S battery performance. In the full cell test, Li was electrodeposited onto Cu/MPC-500 or Cu with an areal charge of 10 mA h cm^{-2} at a current density of 1 mA cm^{-2}. Then the cells were disassembled to get Cu/Li-MPC-500 or Cu/Li. After that, a Li–S battery was fabricated with Al/S-MPC-1300 and Cu/Li-MPC-500 as the cathode and anode, respectively. As a control group, a full cell with the Al/S-CB cathode and Cu/Li anode was prepared.

4.2.4 Material characterization. The morphology of the mesoporous carbon structure and active material before and after cycling was characterized by transmission electron microscope (TEM) (JEOL 1010) and scanning electron microscope (SEM) (Hitachi S4800). Raman spectroscopy was performed on a LabRam HR800 UV NIR with 532 nm laser excitation. Nitrogen adsorption–desorption isotherms were obtained on a Tristar 3000 instrument.

Conflicts of interest

There are no conflicts to declare.

Acknowledgements

H. L. Zhu acknowledges the financial startup support from Northeastern University and financial support from Rogers corporation. We also thank the Kostas Research Institute at Northeastern University and the Center for Nanoscale System (CNS) at Harvard University for using their facilities.

References

1 F. Bonaccorso, L. Colombo, G. H. Yu, M. Stoller, V. Tozzini, A. C. Ferrari, R. S. Ruoff and V. Pellegrini, *Science*, 2015, **347**, 1246501.
2 Y. C. Jiao, D. D. Han, Y. Ding, X. F. Zhang, G. N. Guo, J. H. Hu, D. Yang and A. G. Dong, *Nat. Commun.*, 2015, **6**, 6420.
3 A. Manthiram, S. H. Chung and C. X. Zu, *Adv. Mater.*, 2015, **27**, 1980–2006.
4 D. Lin, Y. Liu and Y. Cui, *Nat. Nanotechnol.*, 2017, **12**, 194.
5 W. Xu, J. L. Wang, F. Ding, X. L. Chen, E. Nasybutin, Y. H. Zhang and J. G. Zhang, *Energy Environ. Sci.*, 2014, **7**, 513–537.
6 D. C. Lin, Y. Y. Liu and Y. Cui, *Nat. Nanotechnol.*, 2017, **12**, 194–206.
7 K. Yan, Z. D. Lu, H. W. Lee, F. Xiong, P. C. Hsu, Y. Z. Li, J. Zhao, S. Chu and Y. Cui, *Nat. Energy*, 2016, **1**, 16010.
8 B. Zhu, Y. Jin, X. Z. Hu, Q. H. Zheng, S. Zhang, Q. J. Wang and J. Zhu, *Adv. Mater.*, 2017, **29**, 1603755.
9 Z. Liang, D. C. Lin, J. Zhao, Z. D. Lu, Y. Y. Liu, C. Liu, Y. Y. Lu, H. T. Wang, K. Yan, X. Y. Tao and Y. Cui, *Proc. Natl. Acad. Sci. U. S. A.*, 2016, **113**, 2862–2867.
10 Z. W. Seh, Y. M. Sun, Q. F. Zhang and Y. Cui, *Chem. Soc. Rev.*, 2016, **45**, 5605–5634.
11 Q. Pang, X. Liang, C. Y. Kwok and L. F. Nazar, *Nat. Energy*, 2016, **1**, 16132.
12 G. Li, J. H. Sun, W. P. Hou, S. D. Jiang, Y. Huang and J. X. Geng, *Nat. Commun.*, 2016, **7**, 10601.
13 R. P. Fang, S. Y. Zhao, P. X. Hou, M. Cheng, S. G. Wang, H. M. Cheng, C. Liu and F. Li, *Adv. Mater.*, 2016, **28**, 3374–3382.
14 A. Manthiram, Y. Z. Fu, S. H. Chung, C. X. Zu and Y. S. Su, *Chem. Rev.*, 2014, **114**, 11751–11787.
15 A. Manthiram, Y. Z. Fu and Y. S. Su, *Acc. Chem. Res.*, 2013, **46**, 1125–1134.
16 A. Rosenman, E. Markevich, G. Salitra, D. Aurbach, A. Garsuch and F. F. Chesneau, *Adv. Energy Mater.*, 2015, **5**, 1500212.
17 M. D. Tikekar, S. Choudhury, Z. Y. Tu and L. A. Archer, *Nat. Energy*, 2016, **1**, 1–7.
18 H. S. Wang, D. C. Lin, Y. Y. Liu, Y. Z. Li and Y. Cui, *Sci. Adv.*, 2017, **3**, 1701301.
19 L. Liu, Y.-X. Yin, J.-Y. Li, N.-W. Li, X.-X. Zeng, H. Ye, Y.-G. Guo and L.-J. Wan, *Joule*, 2017, **1**, 563–575.
20 J. Lang, J. Song, L. Qi, Y. Luo, X. Luo and H. Wu, *ACS Appl. Mater. Interfaces*, 2017, **9**, 10360–10365.
21 G. Zheng, S. W. Lee, Z. Liang, H.-W. Lee, K. Yan, H. Yao, H. Wang, W. Li, S. Chu and Y. Cui, *Nat. Nanotechnol.*, 2014, **9**, 618.
22 J. Xie, L. Liao, Y. Gong, Y. Li, F. Shi, A. Pei, J. Sun, R. Zhang, B. Kong, R. Subbaraman, J. Christensen and Y. Cui, *Sci. Adv.*, 2017, **3**, 3107.
23 S. S. Zhang, *J. Power Sources*, 2013, **231**, 153–162.
24 J. Zhang, Z. Li, Y. Chen, S. Gao and X. W. Lou, *Angew. Chem., Int. Ed.*, 2018, **57**, 10944–10948.

25 Y. Meng, G. Lin, H. Ding, H. Liao and C. Wang, *J. Mater. Chem. A*, 2018, **6**, 17186–17191.
26 J. Song, C. Zhang, X. Guo, J. Zhang, L. Luo, H. Liu, F. Wang and G. Wang, *J. Mater. Chem. A*, 2018, **6**, 16610–16616.
27 H. L. Wang, Y. Yang, Y. Y. Liang, J. T. Robinson, Y. G. Li, A. Jackson, Y. Cui and H. J. Dai, *Nano Lett.*, 2011, **11**, 2644–2647.
28 G. M. Zhou, S. F. Pei, L. Li, D. W. Wang, S. G. Wang, K. Huang, L. C. Yin, F. Li and H. M. Cheng, *Adv. Mater.*, 2014, **26**, 625–631.
29 Z. Yuan, H. J. Peng, J. Q. Huang, X. Y. Liu, D. W. Wang, X. B. Cheng and Q. Zhang, *Adv. Funct. Mater.*, 2014, **24**, 6105–6112.
30 J. C. Guo, Y. H. Xu and C. S. Wang, *Nano Lett.*, 2011, **11**, 4288–4294.
31 N. Jayaprakash, J. Shen, S. S. Moganty, A. Corona and L. A. Archer, *Angew. Chem., Int. Ed.*, 2011, **50**, 5904–5908.
32 X. L. Ji, K. T. Lee and L. F. Nazar, *Nat. Mater.*, 2009, **8**, 500–506.
33 C. Zhang, H. B. Wu, C. Yuan, Z. Guo and X. W. Lou, *Angew. Chem., Int. Ed.*, 2012, **51**, 9592–9595.
34 Y. C. Jiao, D. D. Han, L. M. Liu, L. Ji, G. N. Guo, J. H. Hu, D. Yang and A. G. Dong, *Angew. Chem., Int. Ed.*, 2015, **54**, 5727–5731.
35 M. S. Dresselhaus, A. Jorio, A. G. Souza Filho and R. Saito, *Philos. Trans. R. Soc., A*, 2010, **368**, 5355–5377.
36 H. J. Yu, H. W. Li, S. Y. Yuan, Y. C. Yang, J. H. Zheng, J. H. Hu, D. Yang, Y. Wang and A. G. Dong, *Nano Res.*, 2017, **10**, 2495–2507.
37 G. He, X. Ji and L. Nazar, *Energy Environ. Sci.*, 2011, **4**, 2878–2883.
38 X. Ji, K. T. Lee and L. F. Nazar, *Nat. Mater.*, 2009, **8**, 500.
39 Y. Yang, G. Zheng and Y. Cui, *Chem. Soc. Rev.*, 2013, **42**, 3018–3032.